State Space-Vector Model of Linear Induction Motors Including End-effects and Iron Losses

Part I: Theoretical Analysis

Angelo Accetta, MEMBER, IEEE
National Research Council of Italy (CNR)
Istituto di Ingegneria del Mare (INM)
Palermo, Italy
angelo.accetta@cnr.it

Maurizio Cirrincione, SENIOR MEMBER, IEEE
University of the South Pacific (USP)
School of Engineering and Physics)
Suva, Fiji
maurizio.cirrincione@usp.ac.fj

Marcello Pucci, SENIOR MEMBER, IEEE
National Research Council of Italy (CNR)
Istituto di Ingegneria del Mare (INM)
Palermo, Italy
marcello.pucci@ieee.org

Antonino Sferlazza, MEMBER, IEEE
University of Palermo
DEIM
Palermo, Italy
antonino.sferlazza@unipa.it

***Abstract*— This is the first part of a paper, divided into two parts, dealing with the definition of a space-vector dynamic model of the linear Induction motor (*LIM*) taking into consideration both the dynamic end-effects and the iron losses and its off-line identification. This first part specifically treats the theoretical formulation of this model, which has been expressed in a state form, so to be, in perspective, suitably adopted for developing novel non–linear control techniques, non-linear observers as well as electrical losses minimization techniques (*ELMTs*). Besides the formulation of the dynamic model in space-vector state form, a steady-state analysis is proposed, highlighting the combined effects of the dynamic end-effects and the iron losses on the main electrical quantities of the *LIM*.**

Keywords— Linear Induction Motor (LIM), End-effects, Space-vector, State Model

NOMENCLATURE

$\mathbf{u}_s = u_{sD} + j\,u_{sQ}$ = primary voltages space-vector in the primary reference frame;

$\mathbf{i}_s = i_{sD} + j\,i_{sQ}$ = primary currents space-vector in the primary reference frame;

$\mathbf{i}_r^{'} = i_{rd} + j\,i_{rq}$ = secondary currents space-vector in the primary reference frame;

$\boldsymbol{\psi}_s = \psi_{sD} + j\psi_{sQ}$ = primary flux space-vector in the primary reference frame;

$\boldsymbol{\psi}_r^{'} = \psi_{rd} + j\psi_{rq}$ = secondary flux space-vector in the primary reference frame;

L_s , L_r , L_m = primary, secondary and three-phase magnetizing inductances;

$L_{\sigma s}$, $L_{\sigma r}$ = primary and secondary leakage inductances;

R_s , R_r = primary and secondary resistances;

p = number of pole pairs;

ω_r = angular rotor speed (in electrical angles per second);

v = linear speed;

τ_m = length of the primary;

τ_p = polar pitch.

I. INTRODUCTION

Linear Induction Motors (*LIMs*) have been widely studied because their capability to generate a direct linear motion without the need of any gearbox for the motion transformation (from rotating to linear) [1]-[5]. This positive prerogative of *LIMs* is counterbalanced by several drawbacks, specifically related to such machines. In particular, as for their dynamic modelling, it reveals particularly complex due to the so-called end-effects and border effects. These effects affect significantly the performance of *LIMs* in terms of propulsive force magnitude and its controllability. The existence of such effects calls for suitable models of *LIMs* that can properly account for these effects [6]-[14].

As for some very early works, [6] has proposed a dynamic model of the *LIM*, developed on the basis of the the generalized machine theory by *G. Kron*. Adopting the *Fourier* series space harmonic, the short-stator end-effects have been explained in terms of harmonic asynchronous forces. [7], starting from previous works in the literature, has retained the classical assumption of an effective distribution of sinusoidal rotor windings. As a result, it has used the conventional theory in the calculation of all parameters required in the model. [8] has established the accuracy of the pole-by-pole model by comparing results predicted by the model with the steady-state experimental ones. The key assumption of the pole-by-pole model is that, because of the finite length of the primary, rail poles must be assumed independent and mutually coupled.

Afterwards, [9][10] has proposed a dynamic model of *LIM* whose formulation is based on the machine constructional elements (pole pitch, air-gap length, thickness of the secondary track, slot width and depth, number of turns for phases, etc.). The standpoint of such a model is the definition of a suitable air-gap function, which inherently permits both the static and dynamic end-effects to be accounted. The set of models in [6]-[10] presents, however, the following important drawbacks, that the model proposed in this paper tries to overcome: 1) they are complex and computational demanding to be implemented, 2) their parameterization cannot be easily made with a set of input–output measurements, as classic machine dynamic models, 3) they require several design data, hardly at the disposal of the final user.

The set of dynamic models in [12]-[14] present a more classic space-vector-based approach, taking inspiration from [15]. None of the above cited models, however, takes into consideration either the static end-effects or the transversal edge effects, while they all take into consideration the dynamic end-effects with several approaches.

A further different approach for the dynamic modelling of LIMs has been followed by [17], whose approach is based on the static model proposed in [16]. Specifically, in [16], end-effects and the transversal edge effects are accounted by the definition of specific coefficients multiplying the electrical parameters of the *LIM*. As for the dynamic model in [17], it has proposed a circuital model of the *LIM* based on the winding function method.

More recently, [19][20] has proposed a space-vector dynamic model of the *LIM*, taking into consideration the dynamic end-effects, which has been expressed in a state form and afterwards successfully exploited for the definition of non-linear control techniques suited for *LIMs* [21]-[24], non-linear observers and finally sensorless techniques [25][26]. Such a model presents also the equation of the braking force due to the dynamic end-effects, expressed as a function of the chosen state variables.

None of the above cited dynamic models, however, takes into consideration the iron losses of the *LIM*. Accounting for the iron losses is, in the *LIM* case, even more significant than in the *RIM* (Rotating Induction Motor) case, as explained in section II. To the best of the authors knowledge, only [27] presents a dynamic model and a related control technique of *LIMs* with short secondary which accounts for the iron losses. From the dynamic point of view, however, such a model has the structure of the classic *RIM* model, thus neither the static nor the dynamic end-effects have been accounted for. In [27], a non-linear function is derived from closed-form design calculations and electromagnetic finite-element analysis to properly take into consideration the saturation of the iron core.

This is the first part of a paper, divided into two parts, dealing with the definition of an original space-vector dynamic model of the *LIM* taking into consideration both the dynamic end-effects and the iron losses and its off-line identification. The first part is devoted to the theoretical formulation of the space-vector model of the *LIM* considering both the dynamic end-effects and iron losses as well as to the steady-state analysis and its experimental validation. It highlights the combined effects of the dynamic end-effects and the iron losses on the main electro-mechanical quantities of the *LIM*: propulsive force, magnetic flux and machine equivalent impedance. The proposed dynamic model has been expressed in a state form, so to be, in perspective, suitably adopted for developing novel non-linear control techniques and non-linear observers. The second part is devoted to the development of an identification technique, suitable for the estimation of the model parameters, including the additional ones arising from considering the iron losses as well as to the description of the results validating the proposed model. This paper is an improvement and extension of [28].

In synthesis, the proposed model tries to overcome the most common drawbacks of *LIM* dynamic models:

- It is less complex and computationally demanding than the dynamic models in [6]-[10]. Moreover, differently from them, it can be easily parametrized with input-output tests, without the need of design or constructional data.
- Differently from [6]-[19], besides the dynamic end-effects, it accounts also for the iron losses.

II. State Space-Vector Model of the LIM Including End-effects and Iron Losses

A. Model Assumptions

The proposed space-vector dynamic model of the LIM including the dynamic end-effects and the iron losses is based on the following hypothesis:

- Infinite permeability of iron (no saturation effect is considered);
- Orthogonal direction of the flux density in the air gap;
- Primary slotting effects are neglected;
- Each primary and secondary is considered as a full-pitch multi-turn winding;
- The axes of each primary and secondary three-phase windings are displaced by the angle $2\pi/3$ from each other;
- Dynamic end-effects are considered;
- Static end-effects are not considered;
- Transversal-edge effects are not considered;
- No zero-sequence stator current is present.

Accounting the iron losses is, in the *LIM* case, even more significant than in the *RIM* case. The reason is that, while in the *RIM* the part of the machine that is interested by the rotating air-gap field at supply frequency is the stator core, which is laminated, in the *LIM*, if the moving part is supposed to be the primary, the part interested by the translating air-gap field at supply frequency is the secondary, whose back iron is frequently not laminated. In *LIMs*, thus, differently from *RIMs*, iron losses are concentrated in the secondary track and can be hardly neglected.

A specific consideration must be made with reference to assumption of infinite permeability of the iron. The proposed *LIM* dynamic model inherently does not account for the saturation of the iron core. From this point of view, however, it should be noted that saturation phenomena in *LIMs* are significantly less present than in *RIMs*. This is mainly due to the very large air-gap compared to that typical of a *RIM*, which increases significantly both the reluctance of the main flux path and the leakage flux. In addition, the back iron of the secondary track presents very often a limited thickness, which sometimes is absent at all, further increasing the part of the magnetic circuit not made in ferromagnetic material. With specific reference to the *LIM* under test, the entire magnetic characterization of the machine has been shown in [29]. In particular, [29] has proposed a procedure for identifying the dependences of all the electric parameters of the model from the secondary magnetizing current. Results presented in [29] clearly show that the magnetic saturation does not play a significant role. As a matter of fact, both the primary and the three-phase magnetizing inductances show limited variations with the secondary magnetizing current. Correspondingly, the non-linearity of the *LIM* magnetizing curve is very limited and saturation of the core becomes noticeable only at very high values of the magnetizing current. This justifies the neglection of the magnetic saturation in the proposed model.

B. Dynamic End-effects Modeling

The proposed model, exactly as that in [19][20], takes into consideration the *LIM* dynamic end-effects, while is able to account neither the static end-effects nor the transversal-edge effects. In the following, only some considerations about dynamic end-effects will be given for ease of readiness of the model. For further details, the reader can refer to [19][20].

Differently from the static ones, the dynamic end-effects are generated by the relative motion between the primary and the secondary. Such a motion leads to a decrease of the air-gap flux density at entrance of the motion and to a decrease of it at the exit of the motion. As an overall effect, an average decrease of the magnetization level of the machine occurs as well as an increase of the overall power losses. Such a phenomenon increases at increasing speeds of the primary. In the scientific literature, there are several ways in which such phenomenon has been modeled. One of the most interesting ways is the definition of the a so-called called end effect factor Q [15]:

$$Q = \frac{\tau_m R_r}{\left(L_m + L_{\sigma r}\right) v} \tag{1}$$

Q represents the attitude of the *LIM* to resist the loss of output caused by the end-effects; in this sense, it is inversely proportional to the so-called goodness factor defined in [1][3]. It can be observed that, the higher the machine speed, the higher the air-gap thickness (higher leakage inductance) and the lower the primary length, the lower the factor Q. It means that the end-effects increase with the machine speed, with the air-gap thickness and reduces with the primary length.

Correspondingly, the three-phase magnetizing inductance varies with Q in the following way:

$$\hat{L}_m = L_m\left(1 - f\left(Q\right)\right) \tag{2}$$

with:

$$f\left(Q\right) = \frac{1 - e^{-Q}}{Q} \tag{3}$$

Eq. (2) implies that the inductance virtually reduces with the end-effects resulting in an overall demagnetization of the *LIM*.

A detailed computation of the overall losses of the machine highlights that an additional resistance appears in the transversal branch; this resistance accounts for the additional joule losses in the secondary. This resistance is equal to:

$$\hat{R}_r = R_r f\left(Q\right) \tag{4}$$

C. State Formulation

The space-vector electrical circuit of the *LIM* including the end-effects as well the related dynamic model in state form has been proposed in [19][20]. As an upgrade, in this paper, besides the time-varying electrical parameters accounting for the end-effects, also a further resistance R_0 in the transversal branch is present, taking into consideration the iron losses. According to the definition of all these time-varying parameters, the space-vector equivalent circuit of the *LIM* sketched in Fig. 1 has been deduced expressed in the primary (stator) reference frame, which is different from that of the Rotating Induction Motor (*RIM*) because of the dynamic end-effect terms, but it is also different from that in [19][20], because of the presence of the iron losses term. It should be noted that all the time-varying terms are located in the transversal branch of the electrical scheme. As for the classic space-vector electric circuit of the *RIM*, even if it presents 3 inductances, which would theoretically account for 6 state electrical scalar variables (the mechanical variables are not accounted in the following), the real state scalar variables are 4. This is due to the presence of the node on the transversal branch and the related constraint on the sum of the concurring currents. If the resistance R_0 accounting for the iron losses is to be considered, then the constraint linking together the currents flowing in the 3 inductances is not valid any more. Consequently, the electrical state variables increase from 4 to 6 scalar ones. A possible choice of state variables, particularly suited if the secondary flux oriented control is supposed to be integrated in the drive, is composed by the direct and quadrature components of the primary (stator) currents, the 3-phase magnetizing flux and the secondary (rotor) flux, as follows:

$$\mathbf{x} = \left[i_{sD}\ i_{sQ}\ \ \psi_{md}\ \ \psi_{mq}\ \ \psi_{rd}\ \ \psi_{rq}\right]^T \tag{5}$$

Starting from the electric scheme in Fig. 1, the following space-vector voltage equations can be written on the primary (a) and secondary (b) circuits:

$$\mathbf{u_s} = R_s\mathbf{i_s} + \hat{R}_r\mathbf{i}_m + \frac{d\boldsymbol{\psi}_\mathbf{s}}{dt} = R_s\mathbf{i_s} + \hat{R}_r\left[\mathbf{i_s} + \mathbf{i}_r^{'} - \mathbf{i}_0\right] + \frac{d\boldsymbol{\psi}_\mathbf{s}}{dt} \quad ,$$

$$\mathbf{u}_\mathbf{r}^{'} = R_r\mathbf{i}_r^{'} + \hat{R}_r\mathbf{i}_m + \frac{d\boldsymbol{\psi}_\mathbf{r}^{'}}{dt} - j\,\omega_r\boldsymbol{\psi}_\mathbf{r}^{'} \tag{6 a, b}$$

For the meaning of symbols, the reader can refer to nomenclature at the beginning of the paper.

Eq.s (6 a, b) have been written exploiting the following current balance equation at the node:

$$\mathbf{i}_s + \mathbf{i}_r^{'} = \mathbf{i}_m + \mathbf{i}_0 \tag{7}$$

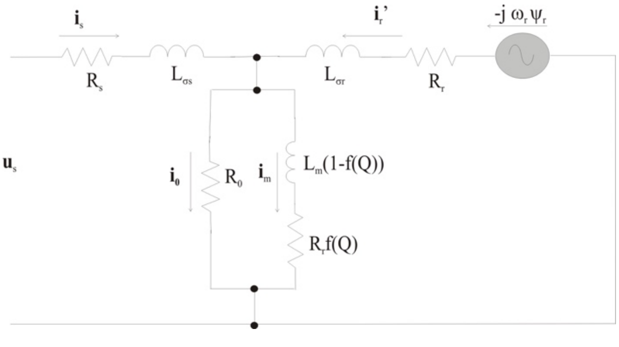

Fig. 1. Space-vector equivalent circuit of the *LIM* including dynamic end effects and iron losses

Eq.s (6 a, b) are different from both the equations of the *LIM* accounting for the end-effects and those of the *RIM* including the iron losses. With respect to the *RIM* model including the iron losses, they include the voltage drop on the variable resistance $\hat{R}_r$ due to the magnetizing current $\mathbf{i}_m$. The flux equations can be written as:

$$\boldsymbol{\psi}_s = L_{\sigma s}\mathbf{i}_s + \hat{L}_m\mathbf{i}_m = L_{\sigma s}\mathbf{i}_s + \boldsymbol{\psi}_m \quad ,$$

$$\boldsymbol{\psi}_r^{'} = L_{\sigma r}\mathbf{i}_r^{'} + \hat{L}_m\mathbf{i}_m = L_{\sigma r}\mathbf{i}_r^{'} + \boldsymbol{\psi}_m \qquad (8\text{ a, b})$$

Even flux equations (8 a, b) are different with respect to the corresponding ones of the *RIM*, for two reasons: firstly, the three-phase magnetizing inductance is a speed-varying quantity, because of the *LIM* end-effects and secondly, the current equation at the node is different because of the presence of the current on the transversal branch resistance R_0 accounting for the iron losses.

A further equation, not present either in classic *RIM* model or in the *LIM* model accounting for the end-effects, is the voltage equation across R_0:

$$\frac{d\boldsymbol{\psi}_m}{dt} + \hat{R}_r\mathbf{i}_m = \frac{d\boldsymbol{\psi}_m}{dt} + \frac{\hat{R}_r}{\hat{L}_m}\boldsymbol{\psi}_m = R_0\,\mathbf{i}_0 \qquad (9)$$

If the secondary current $\mathbf{i}_r^{'}$ is expressed as a function of the three-phase magnetizing and the secondary fluxes, respectively $\boldsymbol{\psi}_m$ and $\boldsymbol{\psi}_r^{'}$, then:

$$\mathbf{i}_r^{'} = \frac{1}{L_{\sigma r}}\boldsymbol{\psi}_r^{'} - \frac{1}{L_{\sigma r}}\boldsymbol{\psi}_m \qquad (10)$$

The current $\mathbf{i}_0$ can be expressed exploiting eq. (7) as a function of the primary current, the three-phase magnetizing and the secondary fluxes:

$$\mathbf{i}_0 = \mathbf{i}_s + \frac{1}{L_{\sigma r}}\boldsymbol{\psi}_r^{'} - \frac{\hat{L}_r}{\hat{L}_m L_{\sigma r}}\boldsymbol{\psi}_m \qquad (11)$$

If eq. (10) is substituted in eq. (9), the following state equation can be written:

$$\frac{d\boldsymbol{\psi}_m}{dt} = R_0\mathbf{i}_s + \left(-\frac{R_0\hat{L}_r}{\hat{L}_m L_{\sigma r}} - \frac{\hat{R}_r}{\hat{L}_m}\right)\boldsymbol{\psi}_m + \frac{R_0}{L_{\sigma r}}\boldsymbol{\psi}_r^{'} \qquad (12)$$

Eq. (12) is the second component of the state model of the machine, where the state variable is the three-phase magnetizing flux $\boldsymbol{\psi}_m$. If R_0 tends to infinity, eq. (12) becomes the static relationship between the three-phase magnetizing flux $\boldsymbol{\psi}_m$ versus the primary current $\mathbf{i}_s$ and the secondary $\boldsymbol{\psi}_r^{'}$.

To obtain the third component of the state model of the *LIM*, eq. (10) is substituted in eq. (6 b) under the assumption $\mathbf{u}_r^{'} = \mathbf{0}$, leading to:

$$\frac{d\boldsymbol{\psi}_r^{'}}{dt} = \left[\frac{R_r}{L_{\sigma r}} - \frac{\hat{R}_r}{\hat{L}_m}\right]\boldsymbol{\psi}_m + \left[-\frac{R_r}{L_{\sigma r}} + j\omega_r\right]\boldsymbol{\psi}_r^{'} \qquad (13)$$

Eq. (13) is the third component of the state model of the LIM, where the state variable is the secondary flux $\boldsymbol{\psi}_r^{'}$. If $\hat{R}_r$ is assumed null, implying that the *LIM* end-effects are neglected, eq. (13) coincides with the rotor equation of the *RIM* including the iron losses, since the three-phase magnetizing flux can be expressed as a function of the primary current and secondary flux on the basis of eq. (9). If R_0 tends to infinity, implying that eq. (9) becomes a static relationship between the three-phase magnetizing flux $\boldsymbol{\psi}_m$ versus the primary current $\mathbf{i}_s$ and the secondary flux $\boldsymbol{\psi}_r^{'}$, eq. (13) coincides with the classic current model of the *RIM*. Finally, if eq. (8 a) is substituted in eq. (6 a), and the derivative of the three-phase magnetizing flux is taken from eq. (12), the following expression of the primary current derivative can be obtained:

$$\frac{d\mathbf{i}_s}{dt} = -\left[\frac{R_s}{L_{\sigma s}} + \frac{R_0}{L_{\sigma s}}\right]\mathbf{i}_s + \frac{R_0\hat{L}_r}{\hat{L}_m L_{\sigma s}L_{\sigma r}}\boldsymbol{\psi}_m - \frac{R_0}{L_{\sigma s}L_{\sigma r}}\boldsymbol{\psi}_r^{'} + \frac{1}{L_{\sigma s}}\mathbf{u}_s \qquad (14)$$

Eq. (14) is the first component of the state model of the *LIM*, where the state variable is the primary current. Eq. (14) coincides with the corresponding state equation of the *RIM* model including the iron losses, excepted that the three-phase magnetizing inductance is a time-varying quantity due to the dynamic end-effects.

The complete state representation of the *LIM* including both the dynamic end-effects and the iron losses can be written as follows:

$$\underbrace{\begin{bmatrix} \dfrac{d\mathbf{i}_s}{dt} \\ \dfrac{d\boldsymbol{\psi}_m}{dt} \\ \dfrac{d\boldsymbol{\psi}_r^{'}}{dt} \end{bmatrix}}_{\frac{d\mathbf{x}}{dt}} = \underbrace{\begin{bmatrix} -\dfrac{(R_s+R_0)}{L_{\sigma s}} & \dfrac{R_0\hat{L}_r}{\hat{L}_m L_{\sigma s}L_{\sigma r}} & -\dfrac{R_0}{L_{\sigma r}L_{\sigma s}} \\ R_0 & -\dfrac{R_0\hat{L}_r}{\hat{L}_m L_{\sigma r}} - \dfrac{\hat{R}_r}{\hat{L}_m} & \dfrac{R_0}{L_{\sigma r}} \\ 0 & \dfrac{R_r}{L_{\sigma r}} - \dfrac{\hat{R}_r}{\hat{L}_m} & -\dfrac{R_r}{L_{\sigma r}} + j\omega_r \end{bmatrix}}_{\mathbf{A}} \underbrace{\begin{bmatrix} \mathbf{i}_s \\ \boldsymbol{\psi}_m \\ \boldsymbol{\psi}_r^{'} \end{bmatrix}}_{\mathbf{x}} + \underbrace{\begin{bmatrix} \dfrac{1}{L_{\sigma s}} \\ 0 \\ 0 \end{bmatrix}}_{\mathbf{b}} \underbrace{\mathbf{u}_s}_{\mathbf{u}} \qquad (15\text{ a})$$

reproducing the classic system equation in state form:

$$\frac{d\mathbf{x}}{dt} = \mathbf{A}\mathbf{x} + \mathbf{b}\mathbf{u} \qquad (15\text{ b})$$

The definition of eq. (15 a) is one of the major contribution of this paper. Fig. 2 shows the entire block diagram of the space-vector model of the *LIM* taking into consideration both the end-effects and the iron losses, expressed in state form. This block diagram properly describes state eq. (15). From the block diagram, the three subsystems describing respectively the primary current, the three-phase magnetizing flux and the secondary flux equations are easily recognizable, as well as the relationships and feedbacks of the state variables.

D. *Mechanical equation*

The mechanical equation of the motion of a *LIM* is:

$$F = F_L + F_r + M\frac{dv}{dt} \qquad (16)$$

where F is the net propulsive force generated by the *LIM*, F_r is the friction force, varying with the speed v by a nonlinear low, F_L is the load force and M is the overall mass of the system (motor plus payload).

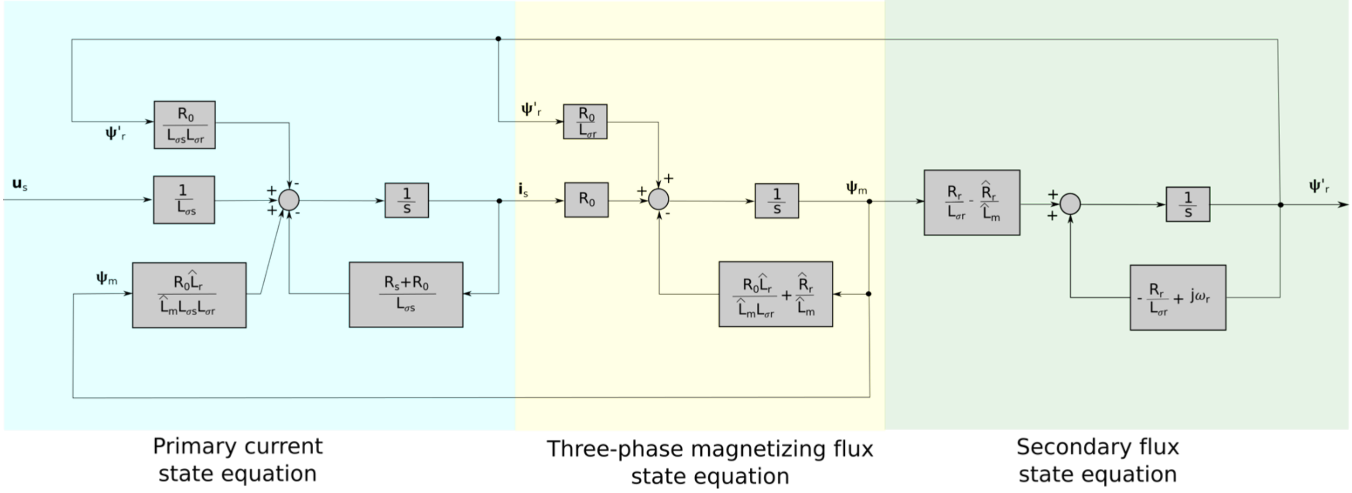

Fig. 2. Block diagram of the *LIM* dynamic model including end-effects and iron losses in the primary reference frame, expressed in state form

Differently from the *RIM* case, in the *LIM* the net thrust is the algebraic sum of the electromagnetic propulsive force F_e (analogous to the torque expression of the *RIM*) and the braking force due to the end-effects F_{eb}.

The mechanical power P_e associated with the electromagnetic force F_e can be written as:

$$P_e = \frac{3}{2}\mathrm{Re}\left(-j\omega_r \boldsymbol{\psi}'_r \mathbf{i}'^{*}_r\right) \tag{17}$$

where the symbol '*' stands for complex conjugate. Taking $\mathbf{i}'_r$ from eq. (8 b) and substituting it into eq. (17), the electromagnetic force is obtained:

$$F_e = \frac{P_e}{v} = \frac{3}{2}\frac{\pi}{\tau_p L_{\sigma r}}\mathrm{Re}\left(j\boldsymbol{\psi}'_r\, \boldsymbol{\psi}^{*}_m\right) \tag{18}$$

Eq. (18) provides the real electromagnetic force produced by the *LIM*, taking into consideration both the iron losses and the dynamic end-effects, and furnishes interesting information. In particular, as far as the field orientation condition is concerned, the maximum force of the *LIM* is obtained boosting the quadrature component of the three-phase magnetizing flux, expressed in the secondary flux oriented reference frame. If R_0 tends to infinite, the force expression in eq. (18) becomes equal to that in [19][20]. The equation of the braking force produced by the *LIM* dynamic end-effects can be retrieved from the expression of the active power dissipated as Joule effect on the additional resistance $\hat{R}_r = R_r f(Q)$ in the transversal branch of the equivalent circuit of the *LIM* (Fig. 1). This power can be written as:

$$P_{eb} = \frac{3}{2}\hat{R}_r\, \Re e\left(\mathbf{i}_m \mathbf{i}^{*}_m\right) \tag{19}$$

where $\mathbf{i}_m$ is the magnetizing current space-vector. Since $\mathbf{i}_m = \frac{\boldsymbol{\psi}_m}{\hat{L}_m}$, it follows that:

$$F_{eb} = \frac{P_{eb}}{v} = \frac{3}{2}\frac{\hat{L}_r}{\hat{L}^2_m}\frac{\left(1-e^{-Q}\right)}{\boldsymbol{\tau}_m}\left|\boldsymbol{\psi}_m\right|^2 \tag{20}$$

Eq. (20) depends on the machine speed, changing its sign with it and being always subtractive with respect to the propulsion force. Moreover, at zero speed, this force is non-null and is proportional to the square of the three-phase magnetizing flux amplitude.

E. Iron Losses Formulation

In general, it can be stated that the iron core losses ΔP_{core} of an *IM*, both the *RIM* and the *LIM* cases, can be divided in two terms, respectively the hysteresis and the eddy current losses, as in the following:

$$\begin{cases} \Delta P_{core\,hyst} = \boldsymbol{\alpha}\, f\, B^x_p \\ \Delta P_{core\,eddy\,curr} = \boldsymbol{\beta}\, f^2\, B^2_p \end{cases} \tag{21 a, b}$$

where B_p is the peak value of the flux density, f is the fundamental frequency, x is the Steinmetz coefficient, α and β are coefficients depending on the material and on the flux density.

In the proposed model, the iron losses have represented in the space-vector electrical circuit of the *LIM* by means of a constant resistance R_0 in the transversal branch. Such an assumption implies a representation of the iron losses with a quadratic dependence from the air-gap flux density and therefore from the three-phase magnetizing flux amplitude, as follows:

$$\Delta P_{core} = \Delta P_{core\,hyst} + \Delta P_{core\,eddy\,curr} = \frac{3}{2}R_0\left|\mathbf{i}_0\right|^2 = \frac{3}{2}\frac{\boldsymbol{\omega}^2_{mm}\left|\boldsymbol{\psi}_m\right|^2}{R_0} \tag{22}$$

where ω_{mm} and $|\boldsymbol{\psi}_m|$ are respectively the angular speed and the amplitude of the three-phase magnetizing flux space-vector.

F. LIM Pole Analysis

Fig. 3 shows the locus of poles of the *LIM* model described by the eigenvalues of the **A** matrix of eq. (15 a). The locus of the poles has been traced considering a set of *LIM* speeds in the range ±10 m/s (slightly higher than the rated speed).

In particular, the following considerations could be made. The poles related to the secondary flux are positioned more on the left than those related to the primary current. It means that the dynamics of the secondary flux is faster than that of the primary current. The real part of such poles is positioned around 500, about 2.5 times higher than the biggest poles of the primary currents, that are around 200. This is the dual situation with respect to the typical *RIM* dynamics and is due to the very low secondary time constant of the *LIM*. It can be explained by the relatively low value of the magnetizing inductance caused by the large air-gap and the relatively high value of the secondary track resistance, caused by the small value of its thickness. As clearly explained in ref. [19][20], the presence of the dynamic end-effects is cause of an increase of the amplitude of the poles for a given speed, in particular for the poles related to the primary current, corresponding to a fastening of the related dynamics caused by the reduction of the transient time constant. At the same time, a reduction of the damping factor occurs, in particular for the poles related to the secondary flux linkage. Furthermore, a couple of additional poles appear, which is related to the dynamics of the three-phase magnetizing flux. Such poles are complex conjugate, presenting a real part higher than those of the primary current and secondary flux poles (due to the higher value of R_0). The real part of such poles is positioned around 10000, about 200 times higher than the biggest poles of the primary currents, that are around 200. It means that the dynamics of the three-phase magnetizing flux is much faster than those of both the primary current and secondary flux. On the basis of the above considerations, the transient validation of the proposed model has not repeated in this paper, since it has already been experimentally performed in [19][20]. The pole analysis emphasizes that the dynamics of the primary currents and secondary flux is negligibly influenced by the presence of the iron losses. This is true, even if iron losses are more present in LIMs than in RIMs. As a matter of fact, R_0 is in the *LIM* case much smaller than that in the *RIM* case (146 Ω in the *LIM* case versus about 1300 Ω in the *RIM* case). The physical explanation of such a small value of R_0 has been given above. Correspondingly, the pole branch of the three-phase magnetizing flux, in the LIM case, presents a real part which is lower than that in the RIM case.

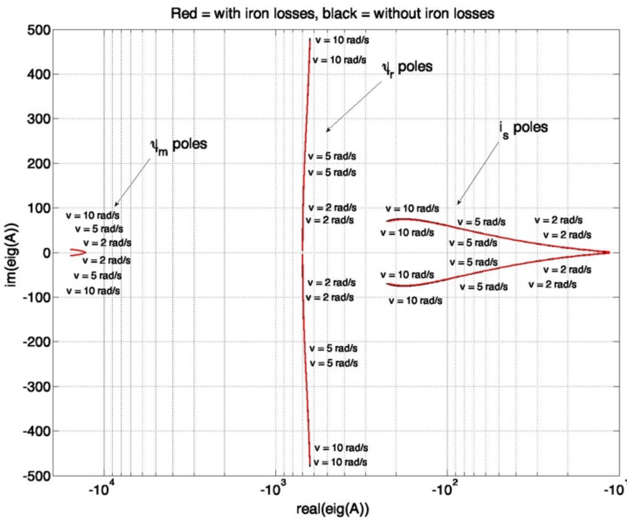

Fig. 3. Poles of the *LIM* model considering both the dynamic end-effects and the iron losses

III. Steady-State Analysis

Starting from the dynamic model described in section II, the steady-state analysis of the *LIM* considering the dynamic end-effects and the iron losses can be made. To perform the steady-state analysis, however, the set of equations (9, 12, 13) must be vector rotated from the primary reference frame to the secondary flux reference frame (all variables in this last reference frame present $\boldsymbol{\psi}_r$ in apex). In such a reference frame, the derivative of all the state variables is null at steady-state, which permits to find out the static relationship between the state variables of the *LIM*. Starting from eq. (12), after the above cited vector rotation and imposing that $d\boldsymbol{\psi}_r^{\psi_r}/dt = 0$, the following relationship between the amplitudes of the secondary flux and the three-phase magnetizing flux holds:

$$\boldsymbol{\Psi}_r^{\psi_r} = \frac{\left[\dfrac{R_r}{L_{\sigma r}} - \dfrac{\hat{R}_r}{\hat{L}_m}\right]}{j(\omega_{mr} - \omega_r) + \dfrac{R_r}{L_{\sigma r}}} \boldsymbol{\Psi}_m^{\psi_r} = \gamma \boldsymbol{\Psi}_m^{\psi_r} \tag{23}$$

where γ is a complex operator depending on the *LIM* speed via $\hat{R}_r$ and on the *LIM* load via the slip speed $\omega_{mr} - \omega_r$.

If eq. (12) is considered, after the above cited vector rotation, exploiting eq. (23) and imposing that $d\boldsymbol{\psi}_m^{\psi_r}/dt = 0$, the following relationship between the amplitudes of the three-phase magnetizing flux and the primary current holds:

$$\boldsymbol{\Psi}_m^{\psi_r} = \frac{R_0}{j\omega_{mr} + \dfrac{R_0 \hat{L}_r}{\hat{L}_m L_{\sigma r}} + \dfrac{\hat{R}_r}{\hat{L}_m} - \gamma \dfrac{R_0}{L_{\sigma r}}} \mathbf{I}_s^{\psi_r} = \delta \mathbf{I}_s^{\psi_r} \tag{24}$$

where δ is a complex operator depending on the *LIM* speed via $\hat{R}_r$ and $\hat{L}_m$, as well as on the supply pulsation via ω_{mr}.

Finally, if (14) is considered, after the above cited vector rotation, exploiting eq.s (23), (24) and imposing that $d\mathbf{i}_s^{\psi_r}/dt = 0$, the following relationship between the amplitudes of the primary current and the primary voltage holds:

$$\mathbf{I}_s = \frac{\mathbf{U}_s}{j\omega_{mr} L_{\sigma s} + R_s + R_0\left(1 - \dfrac{\hat{L}_r}{\hat{L}_m L_{\sigma r}}\delta + \dfrac{1}{L_{\sigma r}}\gamma\delta\right)} \tag{25}$$

From eq. (25), the expression of the equivalent steady-state impedance of the *LIM* can be retrieved as:

$$Z_{eq} = \frac{\mathbf{U}_s}{\mathbf{I}_s} = j\omega_{mr} L_{\sigma s} + R_s + R_0\left(1 - \frac{\hat{L}_r}{\hat{L}_m L_{\sigma r}}\delta + \frac{1}{L_{\sigma r}}\gamma\delta\right) \tag{26}$$

in eq. (26), the dependence of the equivalent impedance Z_{eq} from the *LIM* speed and load is inside the coefficients γ and δ.

If eq.s (23) and (24) are substituted in eq. (18), after expressing the steady state primary current space-vector as a function of the steady-state primary voltage space-vector, the expression of the *LIM* steady-state propulsive force can be found as:

$$F_e = \frac{P_e}{v} = -\frac{3}{2}\frac{\pi}{\tau_p L_{\sigma r}} \mathrm{Im}(\gamma)|\delta|^2 \frac{|\mathbf{U}_s|^2}{|Z_{eq}|^2} \tag{27}$$

Analogously, the steady-state braking force can be computed as:

$$F_{eb} = \frac{3}{2}\frac{\hat{L}_r}{\hat{L}_m^2}\frac{\left(1-e^{-Q}\right)}{\boldsymbol{\tau}_m}\left|\boldsymbol{\delta}\right|^2\frac{\left|\mathbf{U}_s\right|^2}{\left|Z_{eq}\right|^2} \qquad (28)$$

The following results have been obtained adopting, as for the parameters of the above described model, those retrieved with the identification techniques described in [30]. The *LIM* experimental prototype to which the following graphs are related has been fully described in [19] and [30]. Fig. 3 shows the Z_{eq} loci, real part vs imaginary one, for values of the slip ranging between – 1 and 1. Each plot has been drawn for a specific set of supply voltages and frequencies. The ratio between the voltage amplitude and frequency has been kept constant in the different plots (260 V RMS - 60 Hz, 130 V RMS - 30 Hz, 65 V RMS - 15 Hz), excepted for one case related to the field weakening working condition (260 V RMS - 120 Hz). It should be noted that, if the model accounting neither the dynamic end-effects nor the iron losses is considered (blue trace), the Z_{eq} locus is almost symmetrical with respect to the imaginary axis. The higher the supply frequency is, the higher the machine impedance is, as expected. The machine presents its maximum inductive and its minimum resistive behaviours at almost null slip, as expected. Moreover, for negative values of the slip, the machine presents always a negative resistance, connoting the behaviour of the machine as a generator. On the contrary, if the model accounting the dynamic end-effects while not considering the iron losses is considered (green trace), the Z_{eq} locus becomes more asymmetrical with respect to the imaginary axis. Moreover, the higher the supply frequency is (higher steady-state speed), the bigger the difference between the green and blue traces is. In particular, at high supply frequency, the *LIM* exhibits a less inductive behaviour because of the reduction of the three-phase magnetizing inductance due to the dynamic end-effects. Moreover, because of the end-effects, the locus becomes more asymmetrical with respect to the imaginary axis, and it can be explained observing that the end-effects play a major role at super-synchronous speeds. If the model not accounting the dynamic end-effects while considering the iron losses is considered (black trace), the Z_{eq} locus is almost superimposed to the blue trace at low supply frequencies, while becoming different at high supply frequencies, where the iron losses play a more significant role. Moreover, because of the iron losses, the locus becomes more asymmetrical with respect to the imaginary axis, and it can be explained observing that the iron losses play a major role at super-synchronous speeds. If both end effects and iron losses are considered (red trace), the biggest difference with respect to the blue trace is observable, in particular at high supply frequencies and at super-synchronous speeds. In particular, the because of the combined effect of iron losses and end effects, the working region in which the machine behaves as generator reduces significantly, becoming almost null in field weakening region.

Fig. 4 shows the steady-state characteristic, three-phase magnetizing flux versus slip, traced for values of the slip ranging between – 1 and 1. Each plot has been drawn for the same set of supply voltages and frequencies represented in the graphs of the equivalent impedance.

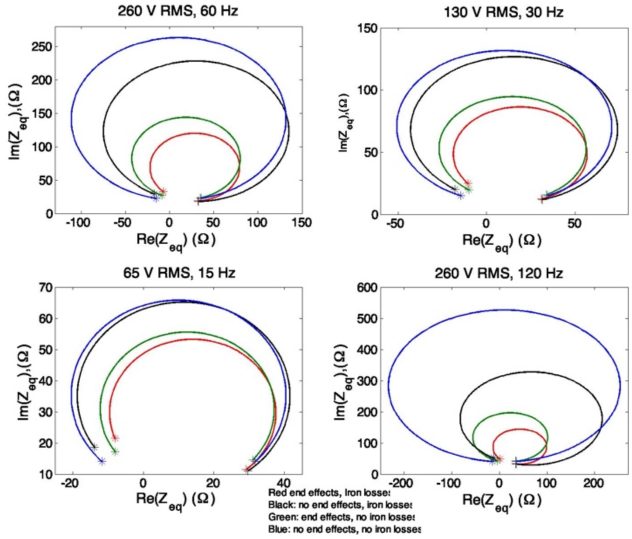

Fig. 4. Steady-state Z_{eq} of the *LIM* ('+' corresponds to s=1. '*' corresponds to s=-1)

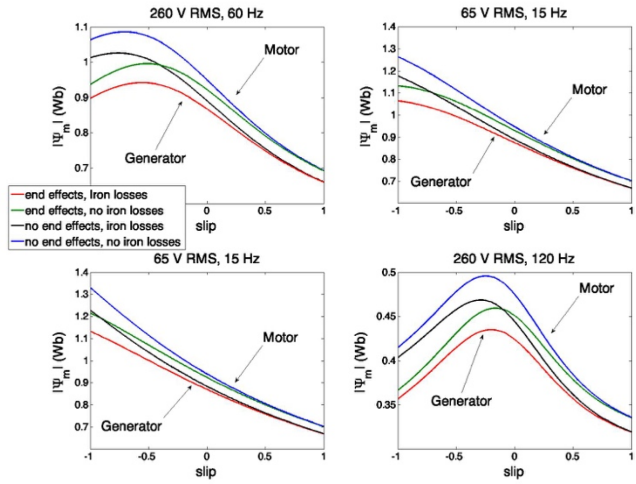

Fig. 5. Steady-state $\left|\boldsymbol{\psi}_m\right|$ vs slip of the *LIM*

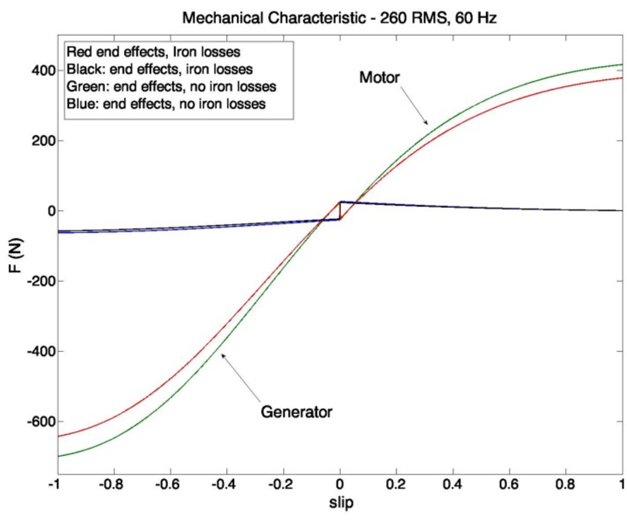

Fig. 6. Steady-state mechanical characteristic force vs slip of the *LIM*

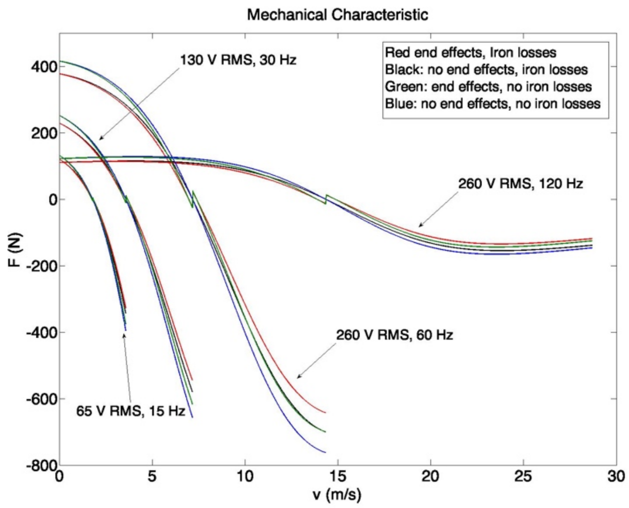

Fig. 7. Steady-state mechanical characteristic force vs speed of the *LIM*

It can be observed that, moving from the working conditions at null slip, a reduction of the three-phase magnetizing flux occurs for increasing values of the slip because of the presence of both iron losses and end-effects, playing the iron losses a major role especially at low supply frequencies. At slip equal to 1, a reduction of three-phase magnetizing flux occurs, caused only by the iron losses, since the end-effects do not play any role. At increasing supply frequencies and super-synchronous speeds, the end-effects tend to play a major role in the flux reduction, especially at high supply frequencies and in particular in field weakening region. Fig. 5 shows the steady-state mechanical characteristic, force versus slip, of the *LIM*, under the supply voltage of 260 V RMS, and frequency of 60 Hz. Such characteristic has been traced twice, respectively considering both the end-effects and the iron losses (red trace) and considering end-effects but neglecting the iron losses (green trace), to highlight just the effect of the presence of the iron losses. The same graph presents also the trace of the end-effects braking force, in the same two cases. As a first major consideration, it can be noted that the mechanical characteristic of the *LIM* prototype under analysis presents an always-decreasing shape with the slip, differently from the classic shape of the *RIM* characteristic. It can be explained considering the high value of the secondary track resistance, due to its limited thickness, as well as the high value of the secondary leakage flux, due to the big air-gap. It can be further noted that the presence of the iron losses causes a strong reduction of the start-up force of the *LIM* (s=1). Moreover, the reduction of the propulsive force is even higher at super-synchronous speed, as expected. The no-load speed of the machine is achieved for a slip value higher than zero, because of the end-effects. The end-effect braking force slightly reduces because of the presence of iron losses, that can be explained with the reduction of the three-phase magnetizing flux in the entire slip range because of the iron losses (see Fig. 4).

Fig. 6 shows a set of mechanical characteristics of the *LIM*, net force versus speed drawn for the same set of supply voltages and frequencies represented in the graph of the equivalent impedance. Results are coherent with those deducible from the analysis of Fig. 5. It must be noted that the net force in generating mode is always much higher than that in motoring mode. The ratio between the peak force amplitudes in generating and motoring modes is, however, much higher at low speeds than at high speed, particularly in field weakening region. This is due to the combined effect of the iron losses and end-effects. In particular, at lower supply frequencies end-effects play a major role in force reduction with respect to iron losses, while it is vice versa at higher supply frequencies. At very low speed, whatever the supply frequency is, the net force reduction is caused mainly by the iron losses.

IV. Steady-State Experimental Validation

As recalled in section II.F, the pole analysis performed on the basis of the proposed dynamic model emphasizes that the transient behavior of the *LIM* is negligibly influenced by the presence of the iron losses. For this reason, the transient validation of the model presented in [19][20] is assumed valid and reliable and will not repeated in the following. Only the steady state experimental validation of the model will be thus shown. As for the *LIM* prototype under test, all the details related to the experimental set-up have been described in [19][20], repeated for the sake of readability in part II of this manuscript. The experimental measurements performed for the validation of the proposed model have required particular care. As a matter of fact, the limited length of the secondary track (1.6 m) has imposed the *LIM* to be supplied at limited values of voltage amplitude and frequency, corresponding to very low values of the no-load speed. The secondary track rail presents, additionally, a very high mechanical friction. To make the experimental results reliable, the PMSM drive adopted as active load has been given, for each measurement, a bias of propulsive reference force exactly equal to the friction force load, in order the friction not influence the measurements and the real mechanical characteristic to be retrieved.

Fig. 8 shows the steady-state equivalent impedance, Z_{eq} , locus under the supply voltage of 30.5 V RMS, 8 Hz. The test has been performed in the entire slip range between 0 and 1. The graph shows the locus obtained with the proposed model as well as the experimental measurements. It can be observed that the experimental points very well track the curve obtained with the model, for the entire range of the slip.

Fig. 9 shows the mechanical characteristic of the LIM, propulsive force versus speed, obtained under the same supply conditions. The test has been performed in the entire slip range between 0 and 1. Even in this case, the graph shows the mechanical characteristic obtained with the proposed model as well as the experimental measurements. It can be observed that the experimental points very well track the curve obtained with the model, for the entire range of the slip. The above two graphs permit the proposed model to be suitably validated.

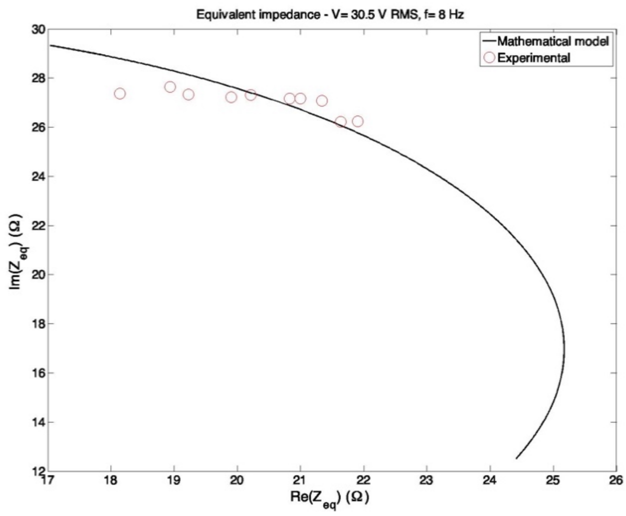

Fig. 8. Steady-state Z_{eq} of the *LIM* – model vs experiments

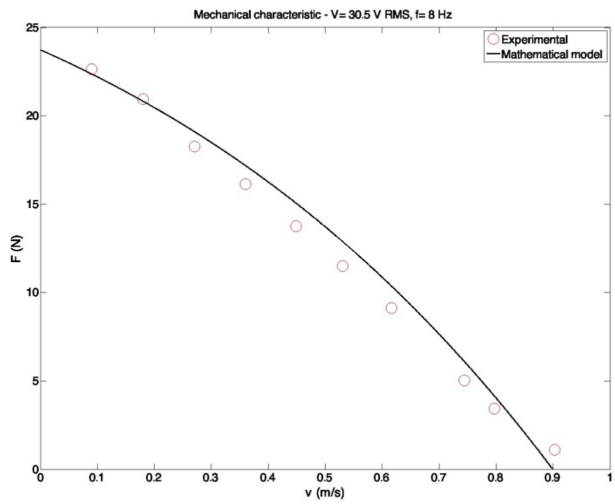

Fig. 9. Steady-state mechanical characteristic force vs speed of the *LIM* – model vs experiments

V. Conclusions

This is the first part of a paper divided in two parts, dealing with the development of a space-vector dynamic model of the *LIM*, which takes into consideration both the dynamic end-effects and also the iron losses. The proposed dynamic model has been expressed in a state form, so to be, in perspective, suitably adopted for developing novel non–linear control techniques and non-linear observers. Besides the formulation of the dynamic model in space-vector state form, a steady-state analysis is proposed, highlighting the combined effects of the dynamic end-effects and the iron losses on the main electrical quantities of the *LIM*. The model has been parametrized and further validated experimentally on a suitably developed test set-up.

References

[1] E. R. Laithwaite: "Linear Electric Machines – A personal view". *Proceedings IEEE*, vol. 63, n° 2, February 1975.

[2] S. Yamamura, *Theory of the Linear Induction Motor*, John Wiley & Sons, 1972.

[3] I. Boldea, S. Nasar, *Linear Electric Motors*, Prentice-Hall inc., 1987.

[4] I. Boldea, S. Nasar, *Linear Motion Electromagnetic Devices*, Taylor & Francis, New York.

[5] I. Boldea, S. A. Nasar, *Linear Electric Actuators and Generators*, Cambridge University Press, 1997.

[6] Boon-Teck Ooi, "A generalized machine theory of the linear induction motor", *IEEE Transactions on Power Apparatus and Systems*, Vol. PAS-92, 1973, pp. 1252-1259

[7] T.A. Lipo, T.A. Nondahl, "Pole-by-pole dq model of a linear induction machine", *IEEE Transactions on Power Apparatus and Systems,* Vol.PAS-98, No.2 March/April 1979, pp. 629-642

[8] T.A. Lipo, T.A. Nondahl, "Transient analysis of a linear induction machine using the d, q pole-by-pole model", *IEEE Transactions on Power Apparatus and Systems*, Vol. PAS-98,No.4 July/Aug 1979, pp. 1366-1374

[9] G. Gentile, N. Rotondale, M. Scarano: "Analisi del funzionamento transitorio del motore lineare", *L'Energia elettrica*, n° 5, novembre 1987.

[10] G. Gentile, N. Rotondale, M. Scarano: "The linear induction motor in transient operation", *L'Energia Elettrica* n° 7-8, 1988.

[11] V. Isastia, G. Gentile, S. Meo, A. Ometto, N. Rotondale, M. Scarano, "A voltage feeding algorithm for vectorial control of linear asynchronous machines taking into account end effect", *Power Electronic Drives and Energy Systems for Industrial Growth,* 1998. Vol.2, pp. 729-734.

[12] H. Sung, and K. Nam "A New Approach to Vector Control for a Linear Induction Motor Considering End Effects ", *Industry Applications Conference, 1999, Conf. Record of the 1999 IEEE Thirty-Fourth IAS Annual Meeting*, 1999 , pp.: 2284 - 2289 vol.4.

[13] G. Kang, K. Nam, "Field-oriented control scheme for linear induction motor with the end effect", *IEE Proc.-Electr. Power Appl.*, Vol. 152, No. 6, November 2005.

[14] E. F. da Silva, E. Bueno dos Santos, P. C. M. Machado, M. A. A. de Oliveira, "Dynamic Model for Linear Induction Motors", *IEEE ICIT 2003*, Maribor, Slovenia, December 2003, pp. 478-482.

[15] Duncan, C. Eng., "Linear induction motor-equivalent- circuit model", *Proc. IEE*, Vol. 130, Pt. B, No. 1, pp. 51-57, 1983.

[16] W. Xu, J. G. Zhu, Y. Zhang, Z. Li, Y. Li, Y. Wang, Y. Guo; Y. Li. "Equivalent Circuits for Single-Sided Linear Induction Motors", *IEEE Transactions on Industry Applications*, vol.: 46, n: 6, November/December 2010, pp. 2410-2423.

[17] W. Xu, J. Zhu, Y. Zhang, Y. Li, Y. Wang, and Y. Guo, "An improved equivalent circuit model of a single-sided linear induction motor," *IEEE Transactions on Vehicular Technology*, vol.59, no.5, pp.2277-2289, Jun. 2010.

[18] W. Xu, G. Sun, L. Wen, W. Wu, and P. Chu, "Equivalent circuit derivation and performance analysis of a single-sided linear induction motor based on the winding function theory," *IEEE Transactions on Vehicular Technology*, vol.61, no.4, pp.1515-1525, May 2012.

[19] M. Pucci, "State space-vector model of linear induction motors," *IEEE Transactions on Industry Applications*, vol. 50, no. 1, pp. 195–207, 2014.

[20] W. Xu, R. Islam, M. Pucci (editors), *Advanced Linear Machines and Drive Systems*, Springer, 2019.

[21] F. Alonge, M. Cirrincione, M. Pucci, A. Sferlazza, "Input-Output Feedback Linearization Control of Linear Induction Motors Including the dynamic End-Effects", *IEEE Transactions on Industry Applications*, Vol. 52, n. 1, January/February 2016, pp. 254-266

[22] F. Alonge, M. Cirrincione, M., Pucci, A. Sferlazza, "Input-output feedback linearizing control of linear induction motor taking into consideration the end-effects. Part I: theoretical analysis". *Control Engineering Practice*, 36, 2015, pp. 133-141.

[23] F Alonge, M. Cirrincione, F. D'Ippolito, M. Pucci, A. Sferlazza, "Adaptive feedback linearizing control of linear induction motor considering the end-effects". *Control Engineering Practice*, 55, 2016, pp. 116-126.

[24] F Alonge, M. Cirrincione, F. D'Ippolito, M. Pucci, A. Sferlazza "Active disturbance rejection control of linear induction motor", *IEEE Transactions on Industry Applications*, 53(5), 2017, pp. 4460-4471.

[25] A. Accetta, M. Cirrincione, M. Pucci, G. Vitale, "MRAS Speed Observer for High Performance Linear Induction Motor Drives based on Linear Neural Networks", *IEEE Transactions on Power Electronics*, vol. 28, n. 1, January 2013, pp. 123-134.

[26] A. Accetta, M. Cirrincione, M. Pucci, G. Vitale, "Neural Sensorless Control of Linear Induction Motors by a Full-Order Luenberger Observer Considering the End Effects", *IEEE Transactions on Industry Applications*, vol. 50, n. 3, May/June 2014, pp. 1891-1904

[27] D. Hall, J. Kapinski, M. Krefta, O. Christianson, "Transient Electromechanical Modeling for Short Secondary Linear Induction Machines", *IEEE Transactions on Energy Conversion*, vol: 23, n. 3, september 2008, pp. 789 – 795.

[28] A. Accetta, M. Cirrincione, M. Pucci, A. Sferlazza, "State Space-Vector Model of Linear Induction Motors Including Iron Losses Part I: Theoretical Analysis", *IEEE Energy Conversione Congress and Expo 2018 (ECCE 18)*, 23-27 September 2018, Portland, USA.

[29] F. Alonge, M. Cirrincione, F. D'Ippolito, M. Pucci, and A. Sferlazza, "Parameter identification of linear induction motor model in extended range of operation by means of input-output data," *IEEE Transactions on Industry Applications*, vol. 50, no. 2, pp. 959–972, Mar./Apr. 2014.

[30] A. Accetta, M. Cirrincione, M. Pucci, A. Sferlazza, "State Space-Vector Model of Linear Induction Motors Including Iron Losses Part II: Model Identification and Results", *IEEE Energy Conversione Congress and Expo 2018 (ECCE 18)*, 23-27 September 2018, Portland, USA.